

MoDi: Unconditional Motion Synthesis from Diverse Data

Sigal Raab¹, Inbal Leibovitch¹, Peizhuo Li²,
Kfir Aberman³, Olga Sorkine-Hornung², Daniel Cohen-Or¹

¹ Tel-Aviv University, ² ETH Zurich, ³ Google Research
sigal.raab@gmail.com

Abstract

The emergence of neural networks has revolutionized the field of motion synthesis. Yet, learning to unconditionally synthesize motions from a given distribution remains a challenging task, especially when the motions are highly diverse. In this work, we present MoDi – a generative model trained in a completely unsupervised setting from an extremely diverse, unstructured and unlabeled motion dataset. During inference, MoDi can synthesize high-quality, diverse motions that lay in a well-behaved and highly semantic latent space. We show that despite the lack of any structure in the dataset, the latent space can be semantically clustered, facilitating various applications including, semantic editing, crowd simulation and motion interpolation. Our qualitative and quantitative experiments show that our framework achieves state-of-the-art synthesis quality that can follow the distribution of highly diverse motion datasets. Code and trained models are available at <https://sigal-raab.github.io/MoDi>.

1 Introduction

The field of motion synthesis includes a wide range of long-standing tasks whose goal is to generate a sequence of temporally coherent poses that satisfy given cues and/or spatio-temporal constraints and importantly, look natural. In particular, learning to synthesize human motion from a given data distribution is a challenging task, especially when the dataset is highly diverse, unstructured and unlabeled. In recent years, deep neural networks have become a popular tool for motion generation, and their excellent performance is imputed to their ability to learn motion priors from large scale datasets. However, learning a motion prior from a diverse dataset remains a challenge.

Previous works focused on synthesizing specific types of motion of limited diversity (Holden, Komura, and Saito 2017), building upon recurrent networks, conditioned by a set of initial frames (Zhou et al. 2018) or learn from a structured dataset and condition the synthesis by a label indicating a specific action (Petrovich, Black, and Varol 2021).

We present MoDi, an unconditional generative model that synthesizes diverse motions. Our model is unsupervised and is trained on diverse, unstructured and unlabeled motion datasets, yielding a well-behaved, highly semantic latent space, which facilitates a variety of synthesis operations.

Our design is inspired by the powerful architecture of StyleGAN (Karras et al. 2020), which has become a foundation for synthesis in the imaging domain, as it learns a

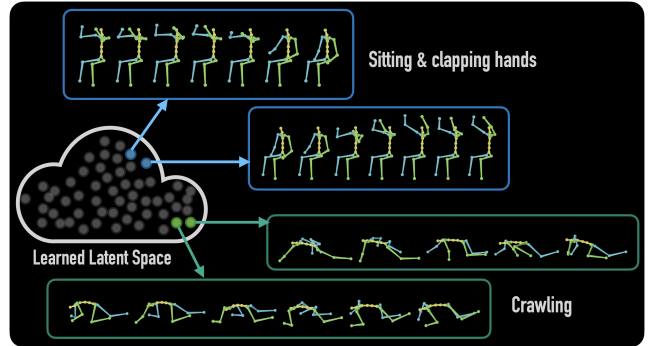


Figure 1: Our generative model is learned in an unsupervised setting from a diverse, unstructured and unlabeled motion dataset and yields a highly semantic, clustered, latent space that facilitates synthesis operations. Note that each single latent code represents a whole motion sequence.

well-structured latent space that allows incredible semantic editing capabilities (Bermano et al. 2022). However, there is a significant gap between the imaging and motion domains; Images possess a regularized 2D spatial structure with a relatively large number of degrees of freedom (DoF), while motion data is irregular, consisting of a skeletal graph with a temporal axis that has a smaller number of DoF. To mitigate this gap and to convert the key-ideas of image-based StyleGAN into the motion domain, we conducted a thorough study of potential architectural variations (order and number of blocks, resolution, layers, etc.), operators (2D vs. 3D convolutions, with and without skeleton-aware operators(Aberman et al. 2020a)), various data representations (positions, rotations, etc.) and ran numerous of experiments. As a result, we have carefully designed a framework that borrows StyleGAN’s style-code injection and mapping elements and is based on 3D skeleton-aware operators convolutions. Furthermore, we introduce a novel filter that replaces skeleton-aware pooling.

Our results show that MoDi learns a structured latent space that can be clustered into regions of semantically similar motions without any supervision. This latent space facilitates applications on diverse motions, including semantic editing, semantic interpolation between motions, and crowd simulation. Furthermore, we present an inversion technique that projects a given motion into latent space, allowing the

usage of our applications on unseen motions. We evaluate our synthesis network qualitatively and quantitatively, and show that it outperforms SOTA methods in similar settings.

Our contribution is threefold: (i) A network that synthesizes diverse natural motions, (ii) an inversion mechanism from real motions to our latent space, and (iii) a novel 3D convolutional filter that replaces skeleton-aware pooling.

2 Related Work

The emergence of neural networks has transformed the field of motion synthesis, and many novel neural models have been developed in recent years (Holden et al. 2015; Holden, Saito, and Komura 2016). Most of these models focus on specific human motion related tasks, conditioned on some limiting factors, such as motion prefix (Aksan, Kaufmann, and Hilliges 2019; Barsoum, Kender, and Liu 2018; Habibie et al. 2017; Yuan and Kitani 2020; Zhang, Black, and Tang 2021; Hernandez, Gall, and Moreno-Noguer 2019), in-betweening (Harvey et al. 2020; Duan et al. 2021; Kaufmann et al. 2020; Harvey and Pal 2018), motion retargeting or style transfer (Holden et al. 2017; Villegas et al. 2018; Aberman et al. 2019, 2020a,b), music (Aristidou et al. 2021; Sun et al. 2020; Li et al. 2021; Lee, Kim, and Lee 2018), or text (Tevet et al. 2022; Zhang et al. 2021).

A large number of models focus on action conditioned generation. These works are closer in spirit with ours, hence in the following we elaborate about them. These models can be roughly divided to autoregressive (Petrovich, Black, and Varol 2021; Fragkiadaki et al. 2015; Zhou et al. 2018; Maheshwari, Gupta, and Sarvadevabhatla 2022; Guo et al. 2020; Habibie et al. 2017; Jang and Lee 2020; Ghorbani et al. 2020) and GAN-based (Degardin et al. 2022; Wang et al. 2020b; Yan et al. 2019; Yu et al. 2020).

Petrovich, Black, and Varol (2021) learn an action-aware latent representation by training a VAE. They sample from the learned latent space and query a series of positional encodings to synthesize motion sequences conditioned on an action. They employ a transformer for encoding and decoding a sequence of parametric SMPL human body models. Maheshwari, Gupta, and Sarvadevabhatla (2022) generate single or multi-person pose-based action sequences with locomotion. They present generations conditioned by 120 action categories. They use a Conditional Gaussian Mixture Variational Autoencoder to enable intra and inter-category diversity. Wang et al. (2020a) employ a sequence of recurrent autoencoders. They replace the KL divergence loss by a discriminator to ensure the bottle neck distribution.

Some GAN-based models are combined with factors that limit their generalization, such as Gaussian processes (Yan et al. 2019) or auto encoders (Wang et al. 2020b; Yu et al. 2020). Degardin et al. (2022) fuse the architectures of GANs and GCNs to synthesise the kinetics of the human body. Like us, they borrow a mapping network from StyleGAN (Karras et al. 2020). However, their model does not utilize important aspects of StyleGAN such as multi-level style injection. As we demonstrate, these aspects significantly ameliorate the quality of the synthesized motions.

Unlike the above conditional models, we present an unconditional method. Only a few works enable pure unconditioned synthesis. Holden, Saito, and Komura (2016) presented a pioneering work in deep motion. They introduce an unconditional autoencoder, which unlike our model, is not

skeleton-aware. Their latent space is not sufficiently disentangled, so they train a separate feed forward network for each editing task, while MoDi performs editing in the latent space with no need to train an additional network.

In order to process motion in a deep learning framework, many existing works convert the motion into a pseudo image, where the joints and time-frames are equivalent to image height and width, and joint features (e.g., coordinates) are equivalent to RGB channels (Holden, Saito, and Komura 2016; Maheshwari, Gupta, and Sarvadevabhatla 2022; Hernandez, Gall, and Moreno-Noguer 2019; Petrovich, Black, and Varol 2021). While this approach is straightforward and intuitive, joints are fundamentally different from image pixels in that they are not necessarily adjacent to each other as pixels are. A partial solution for this problem is presented in Tree Structure Skeleton Image (TSSI) (Yang et al. 2018), where some of the joints are replicated to ensure skeletal continuity in convolution. However, TSSI cannot reflect all neighborhood degrees.

The emergence of Graph-based convolutional networks has been adopted by the motion research community (Yan et al. 2019), since the human skeleton is naturally represented by a graph, where the joints and bones are represented with vertices and edges, respectively. A full motion is then considered as a spatio-temporal graph (Yu et al. 2020; Degardin et al. 2022).

Since a single kernel shared by all joints cannot capture the fine nuances of each joint, more advanced techniques (Aberman et al. 2020a; Yan et al. 2019) exploit the advantage of using finite size skeletons with predefined topology. Each skeletal joint is unique in the way it relates to its neighbors. In our work, we adopt this approach and dedicate a unique kernel for each joint.

3 Model

At the crux of our approach lies a deep generative model trained in an unsupervised manner on an extremely diverse, unstructured, motion dataset. Our network receives a noise vector drawn from an i.i.d Gaussian distribution and outputs a natural, temporally coherent, human motion sequence.

In recent years, generative works in the image domain have attained unprecedented synthesis quality (Brock, Donahue, and Simonyan 2018; Kingma and Dhariwal 2018; Ho, Jain, and Abbeel 2020), and our framework is inspired by one of the prominent methods – StyleGAN (Karras et al. 2020, 2021). However, StyleGAN as is *cannot* be used for motion synthesis since there is a significant domain gap between images and motions that makes the adaptation non-trivial. First, images possess a regularized spatial structure with an inductive bias of pixel neighborhood which is strongly exploited, while motions are irregular, consisting of joints whose features are adjacent in a tensor but are unnecessarily adjacent in the skeletal topology. Second, images has a relatively larger number of DoF comparing to the DoF of motion which is limited by the number of joints.

In order to bridge the gap, our architectural design employs structure-aware neural filters that enable us to cope with the irregular motion representation. Unlike previous works in the domain, we use 3D convolutions rather than 1D or 2D ones, facilitating essential modulation operators with a dedicated kernel for each skeletal joint. In addition,

to compensate for the low number of DoF and prevent overfitting, we engage a hierarchy that is shallower than the one used in the imaging domain.

Next, we discuss our structure-aware modules and network architecture (Section 3), show that our latent space is semantically clustered, present an inversion technique that projects a given motion into the learned latent space, and demonstrate semantic editing capabilities applications (Section 4). Finally, we show quantitative and qualitative evaluation of our framework and compare it to a state-of-the-art alternative (Section 5). We refer the reader to the supplementary video to see the results of our work.

3.1 Motion representation

We describe motion using temporally coherent 3D joint rotations, $\mathbf{R} \in \mathbb{R}^{T \times J \times K}$, where T , J and K are the numbers of frames, joints and rotation features, respectively. Unit quaternions (4D) attain the best empirical results when used for rotation representation. The root joint position is represented by a sequence of global displacements, $\mathbf{P} \in \mathbb{R}^{T \times 3}$. In addition, our network learns to refrain from foot sliding artifacts using binary foot contact labels, $\mathbf{F} \in \{0, 1\}^{T \times 2}$, that are concatenated to the joints axis. We zero-pad the feature dimension of the root location and the foot contact labels to the size of the rotation feature, K , and add an extra dimension, so all entities (\mathbf{R} , \mathbf{P} and \mathbf{F}) possess the same number of features. Altogether we have $\mathbf{R} \in \mathbb{R}^{T \times J \times K}$ (unchanged), $\hat{\mathbf{P}} \in \mathbb{R}^{T \times 1 \times K}$, and $\hat{\mathbf{F}} \in \mathbb{R}^{T \times 2 \times K}$. Once all features share the same size, we concatenate them and obtain the full motion space by

$$\mathcal{M}_{full} \equiv \mathbb{R}^{T \times E \times K}, \quad (1)$$

where $E = J + 3$ is the number of entities (\mathbf{R} , \mathbf{P} and \mathbf{F}).

Let \mathcal{M}_{nat} denote the space of natural motions that are plausible for humans to enact. Each motion $m \in \mathcal{M}_{nat}$ is represented by a tuple, $[\mathbf{R}_m, \hat{\mathbf{P}}_m, \hat{\mathbf{F}}_m]$. Note that the subspace of all human motions, $\mathcal{M}_{nat} \subset \mathcal{M}_{full}$, is extremely sparse, as most of the values in \mathcal{M}_{full} correspond to unnatural or impossible human motions.

Our network has an hierarchical structure in which the represented motion is evolving from coarse motion representation to a finer one. At each level ℓ the number of frames, joints, entities and features is denoted by T_ℓ , J_ℓ , E_ℓ and K_ℓ , respectively. The number of frames T_ℓ increases between two consecutive levels by a factor of 2, and the number of joints increases by an arbitrary factor in order to obtain a meaningful refinement of the skeleton (Aberman et al. 2020a; Degardin et al. 2022).

Additional representation considerations are detailed in Appendix B.1.

3.2 Structure-aware Neural Modules

We consider the human skeleton as a directed graph, where the joints stand for vertices and the bones stand for directed edges. We associate each skeletal joint with the edge that is directed towards it, hence they share the same features. The root joint, to which no edge is directed, is associated with an abstract edge that starts at the origin. In the following we refer to joints and edges seamlessly, according to the context.

Some works (Degardin et al. 2022; Yu et al. 2020) use Graph Convolutional Networks (GCNs) for neural computation. Like GCNs, they employ the same kernels to all graph

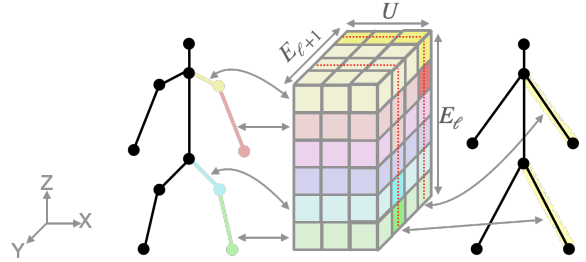


Figure 2: 3D convolutional scaler: Each horizontal slice affects one entity in the fine character (left), and each vertical slice (xz plane) affects one entity in the coarse character (right). Each entity in the coarse character "sees" only weights related to relevant entities of the fine character, emphasised with saturated colors in the filter. Our filter is 5D and since we can only visualize 3D, we omit the channels.

vertices. Unlike general graphs, the topology of the skeleton is known in advance, and has a finite size. These facts can be exploited to get better sensitivity to each joint's unique role in the skeleton. We follow the works that exploit the knowledge of skeletal topology (Yan et al. 2019; Aberman et al. 2020a) and dedicate separate kernels for each joint.

However, these works use naïve pooling to up/down sample the skeletal (spatial) domain. Unpooling uses mere copying and pooling uses averaging. We present a new spatio-temporal convolutional operator, that scales the skeleton topology, as well as the temporal dimension. We use convolution during down-scaling and transposed convolution for up-scaling, both with the same filter architecture. We achieve the desired functionality by adding a dimension to the kernels for the out going joints, similar to the way a dimension is added for the out going channels. The dimensions of each filter are then $K_{\ell+1} \times K_\ell \times E_{\ell+1} \times E_\ell \times U$, where U is the filter width. Figure 2 visualizes our novel convolutional scaler filter and Figure 3 shows how it works.

In addition, we use one existing skeleton-aware module, namely in-place convolution (Aberman et al. 2020a), and add a third dimension to it too. The motivation for 3D is convenience while applying modulation, explained in Appendix B.2. Appendix B.2 also describes skeleton-aware modules in current works (convolutional and pooling).

3.3 Network architecture

Our network receives a noise vector drawn from an i.i.d Gaussian distribution, \mathcal{Z} , and outputs a natural, temporally coherent, human motion sequence, as depicted in Figure 4. Our generator G consists of two main parts: a mapping network that maps noise into a well-behaved, structured, latent space, and a fully convolutional neural network that maps a learned constant and the latent code into the final motion.

Mapping network Let $\mathcal{Z} = \mathcal{N}(\vec{0}, \mathbf{I})$ be a multivariate normal distribution. Given a latent code $z \in \mathcal{Z}$, a non-linear mapping network produces a latent value, $w \in \mathcal{W}$. \mathcal{W} is known to be disentangled and well behaved, as studied by many works (Shen et al. 2020; Nitzan et al. 2021) for images and by Degardin et al. (2022) for motions.

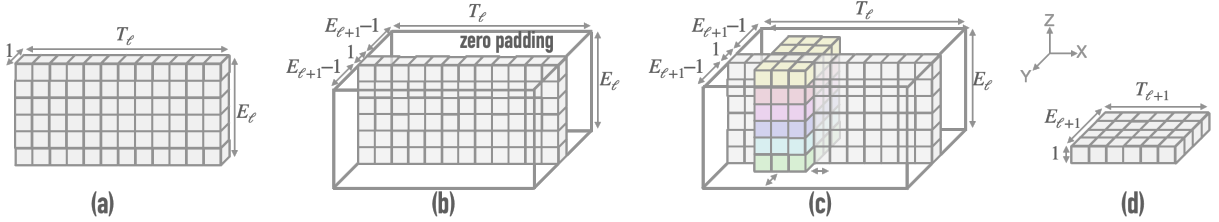


Figure 3: Down sampling with our new filter (depicted 3D out of 4D, no channels): (a) Data at hierarchical level ℓ : Dimensions are $K_\ell \times E_\ell \times T_\ell$. We expand it by one dimension in preparations for 3D convolution. (b) Level ℓ data is further padded by zeros, and its new dimensions are $K_\ell \times (2E_{\ell+1}-1) \times E_\ell \times T_\ell$. (c) 3D convolution: The filter is slid within the data block. Sliding is along the x and y axes only, as the z axis' filter height is identical to the data height. (d) Resulting data: The extra dimension of size 1 is dropped such that final dimensions at level $\ell + 1$ are $K_{\ell+1} \times E_{\ell+1} \times T_{\ell+1}$.

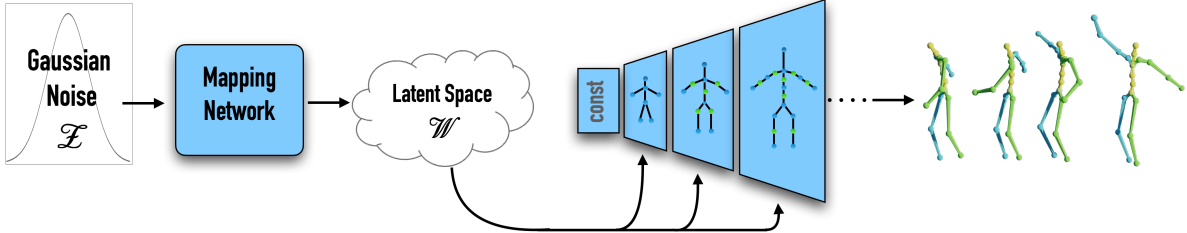


Figure 4: Our motion generator combines structure-aware neural modules with a mapping network and style-codes injected to multiple levels of the generator. A detailed description of the architecture (layers, hyperparameters, ...) is given in the appendix.

Motion synthesis network In this part, we introduce a hierarchical framework that learns to convert a learned constant tensor into a motion representation via a series of skeleton-aware convolutional layers (Section 3.2), where the traditional skeletal pooling layer is replaced by our novel convolutional scaler. The layers in the motion synthesis network are modulated by style-codes that are injected in each level and modify second order statistics of the channels, in a spatially invariant manner (Huang and Belongie 2017). The style codes are learned from the outputs of the mapping network, using affine transformation.

We employ a discriminator (Goodfellow et al. 2014), D , that holds the reverse architecture of the synthesis network. It receives generated or real motion, and processes it in skeleton-aware neural blocks that downscale gradually. A recap of StyleGAN, and details on training setups and hyperparameters, are given in Appendices B.3 and D.2, respectively.

3.4 Loss Functions

Our main loss is adversarial. In addition, we regularize the generator with foot contact and with path length, and regularize the discriminator with $R1$.

Adversarial loss We train our GAN with a non-saturating adversarial loss (Goodfellow et al. 2014),

$$\mathcal{L}_{adv}^G = - \mathbb{E}_{z \sim \mathcal{Z}} [\log D(G(z))], \quad (2)$$

$$\mathcal{L}_{adv}^D = - \mathbb{E}_{m \sim \mathcal{M}_{nat}} [\log D(m)] - \mathbb{E}_{z \sim \mathcal{Z}} [\log(1 - D(G(z)))] . \quad (3)$$

Foot contact loss Accurate foot contact is a major factor of motion quality. There is already special care for foot contact in the adversarial loss, as \mathcal{M}_{nat} contains foot contact labels. However, we noticed that encouraging the contact between the feet and the ground improves the naturalness of

the motions, and discourages the phenomenon of ‘floating’ feet. Hence, we add an encouragement regulation

$$\mathcal{L}_{touch}^G = \mathbb{E}_{z \sim \mathcal{Z}} [-\log s(G(z)_F)], \quad (4)$$

where $(\cdot)_F$ is the contact-label component of the motion, and $s(\cdot)$ is the sigmoid function.

In addition we use contact consistency loss (Li et al. 2022; Shi et al. 2020), which requires that a high velocity should not be possible while a foot is touching the ground:

$$\mathcal{L}_{fcon}^G = \mathbb{E}_{z \sim \mathcal{Z}} \left[\left\| FK(G(z))_f \right\|_2^2 \cdot s(G(z)_F) \right], \quad (5)$$

where $FK(\cdot)$ is a forward kinematic operator yielding joint locations, and $(\cdot)_f$ is feet velocity extracted from them.

Although our foot contact losses notably mitigate sliding artifacts, we further clean foot contact with a fully automatic procedure using standard IK optimization (Li et al. 2022).

Path length loss This loss (Karras et al. 2020) requires that a fixed-size step in \mathcal{W} results in a non-zero, fixed-magnitude change in the generated motion.

$$\mathcal{L}_{path}^G = \mathbb{E}_{w \sim \mathcal{W}, r \sim \mathcal{R}} \left[\left\| J_w^T G(w) * r \right\|_2 - a \right]^2, \quad (6)$$

where \mathcal{R} is a unit Gaussian space normalized by the number of joints and frames, $J_w = \partial G(w)/\partial(w)$, and a is the accumulated mean gradient length.

R1 loss This loss (Mescheder, Geiger, and Nowozin 2018) improves the functioning of the discriminator:

$$\mathcal{L}_{R1}^D = \mathbb{E}_{m \sim \mathcal{M}_{nat}} \left[\left\| \nabla_m D(m) \right\|_2^2 \right]. \quad (7)$$

Altogether, the generator and discriminator losses are

$$\mathcal{L}^G = \mathcal{L}_{adv}^G + \lambda_{touch} \mathcal{L}_{touch}^G + \lambda_{fcon} \mathcal{L}_{fcon}^G, \quad \mathcal{L}^D = \mathcal{L}_{adv}^D. \quad (8)$$

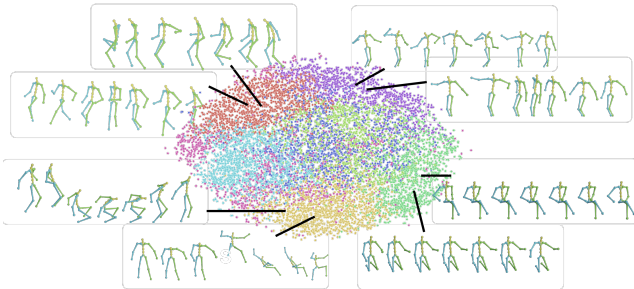


Figure 5: The latent space \mathcal{W} , split into 8 clusters using K-means, and visualized using T-SNE. Each point relates to one \mathcal{W} space instance, generated from random noise $z \in \mathcal{Z}$. The visualized motions are the result of running these latent variables through our generator G . We observe that the clusters indeed represent semantic grouping of the data.

We activate the regularizations \mathcal{L}_{path}^G and \mathcal{L}_{R1}^D in a lazy fashion, as done by Karras et al. (2020).

4 Latent Space Analysis and Applications

4.1 Latent Clusters

We demonstrate that \mathcal{W} is well structured by clustering it into meaningful collections of motions. Recall that MoDi learns diverse datasets, whose data is unstructured and cannot be semantically clustered using common attributes.

In Figure 5 we observe the latent space \mathcal{W} , split into 8 clusters using K-means. The \mathcal{W} values belong to 10,000 randomly synthesized motions. We randomly choose several motions from each cluster and depict them. Clearly, motions represented by different clusters are semantically different, and motions that share a cluster are semantically similar.

4.2 Latent interpolation

Let \bar{w} be the mean of all $w \in \mathcal{W}$, and let *mean motion* denote $G(\bar{w})$, the motion generated by it. The mean motion is depicted at the bottom row of Figure 6(a). This motion is similar for all variations of trained networks, and is what we intuitively expect: an idle standing, front facing character.

We demonstrate the linearity of the latent space \mathcal{W} by interpolating between the latent values and observing the motions generated out of the interpolated values. A special case, called *truncation*, is when the interpolation target is \bar{w} . In the imaging domain, truncation has an important role in regularizing out of distribution images. We show that truncation works well in our model too. A truncated sequence is denoted by $w_i = \hat{w} + \frac{i}{C}(\bar{w} - \hat{w})$, where $\hat{w} \in \mathcal{W}$, C is the number of interpolation steps, and $i \in [0 \dots C]$. Clearly $w_0 = \hat{w}$ and $w_C = \bar{w}$. We can replace \bar{w} by any sampled $\tilde{w} \in \mathcal{W}$, and then the sequence is called interpolated rather than truncated. Let $m_i = G(w_i)$ denote the motion generated out of each w_i . Figure 6 (a) and (b) shows the motions created out of truncation and interpolation, respectively.

We observe favorable characteristics in all interpolation sequences. First, m_i is semantically similar to m_{i-1} , but it also changed towards the semantics of the target m_C . When dealing with truncation, m_i is always milder than m_{i-1} .

Second, we notice that the interpolation is between whole sequences rather than frames. For example, if in m_{i-1} the

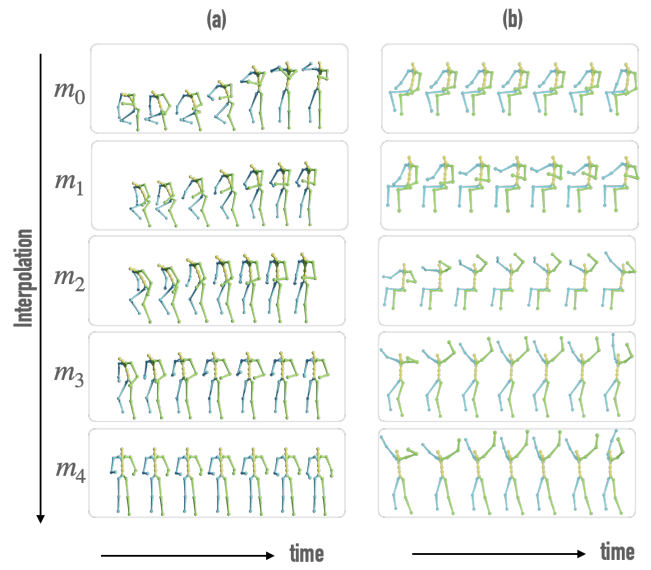


Figure 6: Latent space interpolation with $C = 4$. Col. (a): interpolation to the mean motion (truncation); col. (b): interpolation between two sampled motions. The interpolated motion is notably smooth and natural.

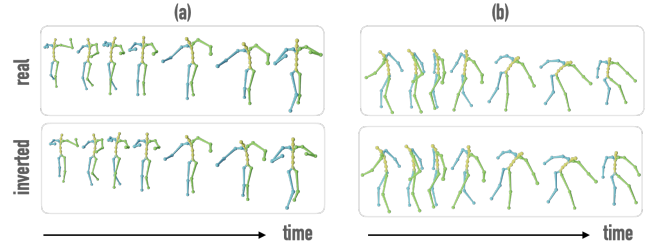


Figure 7: Inversion of two motions, (a) and (b). The original and the reconstructed motions are depicted at the top and bottom rows, respectively. The reconstructed motions are created by first converting the real motions into \mathcal{W}^+ and then running the obtained latent values in the generator.

character jumps occasionally, then in m_i the character jumps in a similar frequency, but unnecessarily on the same frames.

Lastly, there are no unnatural motions in the sequence, although using simple geometric joint interpolation would have resulted in unnatural motions. Figure 6(b) demonstrates this, where our latent interpolation yields natural motions at all stages. A naïve geometric interpolation of edge rotations would result in abnormal pose between sitting to standing, with a vertical spine (see supplementary video).

4.3 Motion Inversion

Our inversion module, I , is an optimizer that gets an input motion m and outputs a latent variable w , where the difference between $G(w)$ and the target motion m is minimized:

$$I(m) = \arg \min_w \|G(w) - m\|_2 + \lambda_{FK} \|FK(G(w)) - FK(m)\|_2. \quad (9)$$

We use gradient descent to minimize the target similarity metric starting with a random Gaussian noise. Inversion quality improves when using \mathcal{W}^+ and when using an $L2$ loss on both rotation angles and joint locations. \mathcal{W}^+ (Ab-

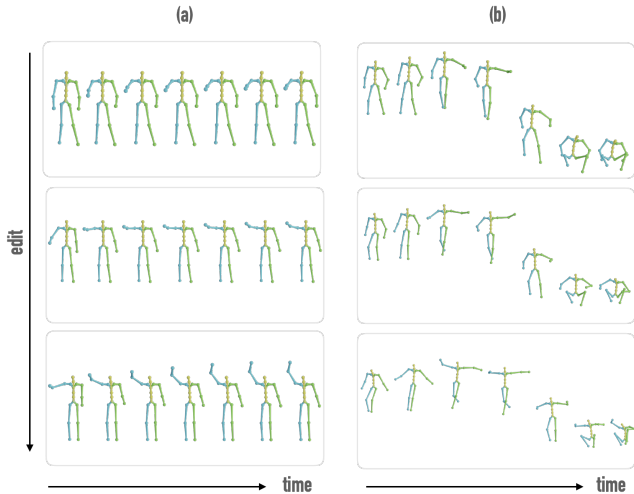


Figure 8: Editing in the latent space. The motion remains intact except for the edited attribute, *gradual right arm lifting* (*gral*). Note that character’s right arm is to the reader’s left. The *gral* attribute gets stronger as we go down in each column. The generative prior of MoDi keeps the jumping motion (b) natural, even at the expense of arm lifting.

dal, Qin, and Wonka 2019) is explained in Appendix C.1.

Figure 7 visualizes the quality of the obtained inversions. Inversion is an important basis for further applications. Once an unseen motion is inverted to the \mathcal{W}^+ space, it can be, for example, semantically edited, as shown next.

4.4 Editing in the latent space

If a latent space is sufficiently disentangled, it should be possible to find direction vectors that consistently correspond to individual factors of variation. Let a be an attribute related to motion. a can be any semantic attribute, such as motion speed, verticality measurement of parts in the body, or a motion style. Inspired by Shen et al. (2020), we compute a score that measures a in a motion. For example, when measuring the verticality of a motion, a character doing a handstand would get a score of -1 , lying down would get a score of 0 , and standing up would get a score of 1 . Using a given score, we train an SVM, yielding a hyperplane that serves as a separation boundary. Denote the unit normal of the hyperplane by n . Then $G(w + n)$ possesses increased score of attribute a comparing to $G(w)$. The only attribute that should change in such editing is a , preserving the rest of the motion intact.

Unlike image datasets, that hold labeling for various attributes (age, gender,...), there is not much labeling in motion datasets. We create our own simple classifiers, and elaborate next regarding one of them, measuring *gradual right arm lifting*, denoted *gral*. *Gral* means that the right arm is lifted as time advances. Computing a score for the *gral* attribute is not straight forward, and is detailed in Appendix C.2. Our results are visualized in Figure 8, where we show that the *gral* attribute gets stronger while stepping in the latent space, and the naturalness of motions as well as their semantics are kept. In our video clip we show that when such an attribute is artificially applied via geometric interpolation, the results are unnatural. Obtaining manual natural results would require an artist’s hard work.

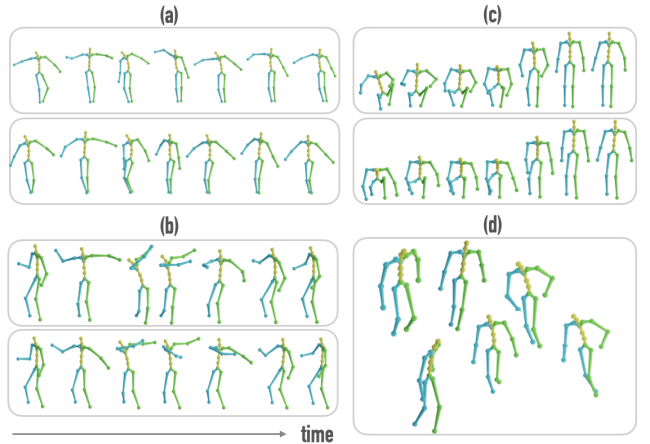


Figure 9: Crowd simulation. Each frame in blocks (a), (b) and (c) depicts a sequence of poses over time of one motion. The two sequences in each of these blocks visualise similar motions created using perturbation in the latent space. Block (d) depicts poses in *one* time frame extracted from six *distinct* motions. (a) a group of dancers; (b) friends playing ‘throw the ball’; (c) an audience standing up to greet an honored guest; (d) crowd strolling in the town square.

4.5 Crowd simulation

Given an input motion m , we can sample variations in our latent space \mathcal{W} by simply sampling the neighborhood of the w that corresponds to m . We sample in a Gaussian $\sim \mathcal{N}(m, \sigma^2)$, with σ in the range 0.1-0.8. This way, one can simulate, for instance, people walking in the town square, a group of dancers, or a group of friends jumping from a high step. See Figure 9 and our video for examples.

5 Experiments

Datasets We use Mixamo (Adobe Systems Inc. 2021) for training and evaluation, and use HumanAct12 (Guo et al. 2020) for evaluation, as described in Appendix D.1.

5.1 Quantitative Results

Metrics We use the metrics FID, KID, precision-recall and diversity, and describe them in Appendix D.3. Some of the other metrics in the literature, e.g., accuracy, cannot be used for an unconstrained model and are hence ignored. The metrics build upon the latent features of an action recognition model. However, training such a model on Mixamo is challenging, as there is no action labeling in it.

Our approach to this challenge is interdisciplinary. Mixamo has a textual label for each motion. Using the Sentence-BERT (Reimers and Gurevych 2019) NLP model, we attain latent features representing the textual characteristics of each motion. Then we use K-means to cluster the embedding, and use each cluster as a pseudo action label. With labels at hand, we train an action recognition model (Yan, Xiong, and Lin 2018). The features extracted from this trained model are then used for metrics calculation.

Results MoDi is unique compared to other works, as it is trained without any constraints. Holden, Saito, and Komura (2016) introduced unconstrained training, but we prefer comparing with more recent works, and since they are all

Model	FID ↓	KID ↓	Precision ↑ Recall ↑	diversity ↑
ACTOR (2021) unconstrained	48.8	0.53	0.72, 0.74	14.1
ACTOR (2021) constrained	18.8	0.18	0.70, 0.56	17.52
MoDi (ours) with mixing	15.55	0.14	0.72 , 0.75	17.36
MoDi (ours) without mixing	13.03	0.12	0.71, 0.81	17.57

Table 1: Quantitative results for state-of-the-art ACTOR and MoDi on the HumanAct12 dataset. The grayed lines show the original algorithms, without the changes that make them comparable. Note that our model leads in all the variations.

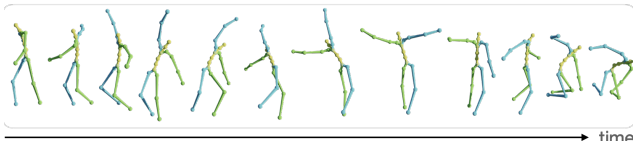


Figure 10: Qualitative result. More are in the video and in Appendix D.4.

conditioned, we make minor changes in the training procedure to make the models comparable, as detailed next.

Changes to constrained models: We ‘convert’ these models to unconstrained ones by assigning the same label to all motion instances, as if they all belong to the same class.

Changes to MoDi: MoDi uses style-mixing (Karras et al. 2020), which encourages disentanglement between hierarchical layers. However, mixing may change the distribution of synthesised motions, yielding degradation in the metric score. Hence, for the sole purpose of comparison with other works, we train our model with no mixing.

We compare our model with state-of-the-art action synthesis network, ACTOR (Petrovich, Black, and Varol 2021), on the HumanAct12 (Guo et al. 2020) dataset. See results in Table 1. We compare to two trained versions of ACTOR. The first, is where we make ACTOR comparable to MoDi by removing the action constraints. The second, used only as a sanity check, is where we run the constrained model provided by the authors. We provide results for two variations of our trained model. The first, is our regular setting, trained with style-mixing. The second is the one that should be compared to action synthesis models, with no mixing. Both versions of MoDi outperform both versions of ACTOR.

5.2 Qualitative Results

The reader is encouraged to watch our supplementary video in order to get the full impression of the quality of our results. For completeness, we show one special motion in Figure 10, and several more in Appendix D.4.

5.3 Ablation

In Table 2 we show the results of a thorough study of potential architectures. We first show the metric scores when using

Architecture variation	FID ↓	KID ↓	Precision ↑ Recall ↑	diversity ↑
non skel.-aware	23.0 ± 0.3	0.17 ± 0.02	0.46 ± 0.01 0.41 ± 0.01	13 ± 0.08
joint loc. rather than rot.	17.3 ± 0.06	0.2 ± 0.03	0.46 ± 0.02 0.58 ± 0.01	14.0 ± 0.3
pool rather than conv. scaler	14.9 ± 0.7	0.16 ± 0.02	0.49 ± 0.01 0.58 ± 0.03	15.3 ± 0.02
remove one in-place conv. per hierarchy	14.1 ± 1.4	0.15 ± 0.02	0.46 ± 0.02 0.66 ± 0.1	15.4 ± 0.9
final architecture	11.5 ± 0.9	0.1 ± 0.01	0.46 ± 0.02 0.69 ± 0.02	15.4 ± 0.2

Table 2: Quantitative results for various generator designs, on the Mixamo dataset. Best scores are emphasised in **bold**.

a non skeleton-aware architecture. That is, when representing motion by pseudo images. The drawbacks of pseudo-images are detailed in Section 2. In the second study, we use joint locations rather than rotations. In the appendix we describe why generating rotations is better than generating locations. Our third study refrains from using our new convolutional scaler, and uses skeleton-aware pooling (Aberman et al. 2020a), testifying that our new filter improves the results. Next, we check what happens when removing one in-place convolution from each hierarchical layer. Finally, we measure the scores for our final architecture, and conclude that our architectural choices outperform other alternatives.

Since our training and evaluation incarcerated randomness (e.g., initialization, stochastic gradient decent, noise sampling, etc.), we have ran every training configuration 3 times, and every evaluation (per training) 5 times. The numbers in Table 2 depict the mean and standard deviation of all the evaluations, formed $mean \pm std$.

6 Conclusion

One of the most fascinating phenomena of deep learning is that it can gain knowledge, and even learn semantics, from unsupervised data. In this work, we have presented a deep neural architecture that learns motion prior in a completely unsupervised setting. The main challenge has been to learn a generic prior from a diverse, unstructured and unlabeled motion dataset. This necessarily requires a careful design of a neural architecture to process the unlabeled data. We have presented MoDi, an architecture that distills a powerful, well-behaved latent space, which then facilitates downstream latent-based motion manipulations.

Like any data-driven method, the quality of the generalization power of MoDi is a direct function of the training data, which, at least compared to image datasets, is still lacking. Another limitation is that skeleton-aware kernels, with dedicated kernels per joint, occupy large volumes, resulting in relatively large running time.

A challenging research direction is to enable learning motion priors from videos. Building upon networks like MoDi, with inductive bias, may open the way towards it.

7 Acknowledgments

This work was supported in part by the Israel Science Foundation (grants no. 2492/20 and 3441/21).

Appendix

A Outline

This Appendix adds details on top of the ones given in the main paper. While the main paper stands on its own, the details given here may shed more light. The majority of this Supplementary recaps non-novel algorithmic elements that are used by our work.

In Appendix B we provide more details regarding our model; considerations that led us to choosing edge rotation representation, description of skeleton aware models in current works, and more details on the StyleGAN architecture. Appendix C describes the \mathcal{W}^+ space used for inversion, and the computation of the *gral* score, used for latent motion editing. Lastly, in Appendix D we elaborate on our experiments; We describe the datasets that we use, provide implementation details such as hyper-parameters, detail metrics and show additional qualitative results.

B Model – Additional Details

B.1 Motion Representation Considerations

Some methods generate a sequence of 3D poses (Degardin et al. 2022), where each location is specified by the 3D coordinates of each joint. However, the resulting representation is incomplete, since it does not reflect a rotation of a bone around its own axis. In particular, it does not contain all the information necessary to drive a rigged virtual 3D character, and the temporal consistency of the skeleton’s bone lengths is not guaranteed. While joint rotations may be recovered from joint positions via inverse kinematics (IK), the solution is not unique, and thus ill-posed. Furthermore, models that predict positions tend to yield a temporally jittery output, and require a post processing smoothing stage. Due to these considerations, we follow numerous recent works that are based on joint rotation representation (Maheshwari, Gupta, and Sarvadevabhatla 2022; Li et al. 2022; Tevet et al. 2022). The motion generated by MoDi can be directly converted into an animation sequence without the need to apply neither IK nor temporal smoothing.

Our network is trained on a single set of bone lengths. Once a motion is generated, it can be retargeted to any other set of bone lengths using existing motion retargeting methods (Aberman et al. 2020a,b; Biswas et al. 2021).

B.2 Structure-aware Neural Modules – Additional Details

In this section we describe skeleton aware neural modules from current works, for information completeness. The modules described here are skeletal in-place convolution and skeletal pooling (Degardin et al. 2022; Yu et al. 2020; Yan et al. 2019; Aberman et al. 2020a). In our work we create a 3D version of the skeletal in-place convolutional filter, and replace the skeletal pooling by our novel convolutional scalar filter.

In Figure 11 we show a skeletal pooling procedure. Pooling is done by averaging the features of two entities, hence, it is equivalent to a convolution with weights of 0.5. Our new filter applies a convolution with learned weights, generalizing the pooling functionality, and allowing the network the freedom to choose the optimal weights.

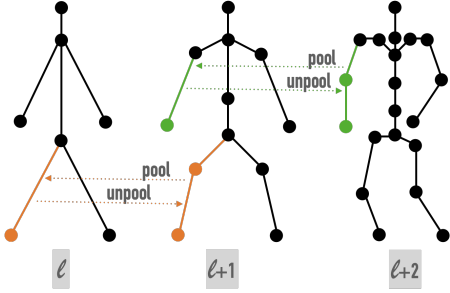


Figure 11: Skeletal pooling, not used by MoDi. The pooling operation merges two adjacent edges and removes the joint between them. The unpooling operation splits an edge into two, and adds a joint between the newly created edges. We denote skeletal hierarchy levels with $\ell, \ell + 1, \ell + 2$, and demonstrate pooling and unpooling on selected joints in orange (levels $\ell, \ell + 1$), and in green (levels $\ell + 1, \ell + 2$).

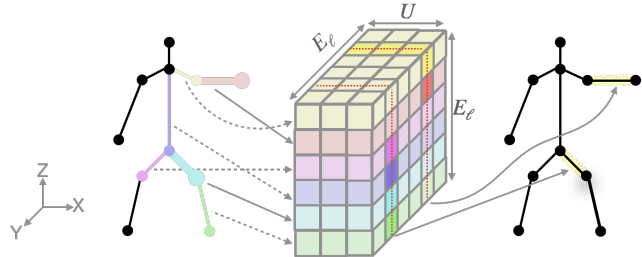


Figure 12: Our 3D version of a skeleton-aware in-place convolutional filter. Each horizontal slice (xy plane) is related to one entity in the input character (left), and each vertical slice (xz plane) is related to one entity in the output character (right). Each entity in the output character “sees” only weights related to its neighboring entities, emphasised with saturated colors in the filter. We demonstrate convolutions on the left thigh and on the left forearm, marked yellow in the output character. Note that each of these entities is affected by its immediate neighbors and ignores entities that do not neighbor it. Our filter is 5D and since we can only visualize 3D, we omit the channels. Recall that E , ℓ , and U denote the number of entities, the hierarchical level index, and the kernel width, respectively.

In Figure 12 we depict our 3D version of a skeleton-aware convolutional filter. Unlike our novel convolutional scaler filter, this filter is an in-place one, which means it retains the dimensions of its input, and cannot scale it.

Motivation for using 3D convolutions Current works use 2D and even 1D in-place skeletal convolutions, where they combine the joints and the channels into the same dimension. Such a combination is not intuitive and moreover, it introduces complications when using modulation, since the style (i.e., new standard deviation) is injected to each channel separately (see Appendix B.3). By using 3D convolutions we place the channels in their own dedicated dimension (as done in most neural architectures), so modulation becomes simple. Skeleton aware convolutions in current works are done with 3D filters of dimensions $(K_{\ell+1} \cdot E_{\ell+1}) \times (K_\ell \cdot E_\ell) \times U$, while MoDi uses 5D filters of dimensions $K_{\ell+1} \times K_\ell \times E_{\ell+1} \times E_\ell \times U$. Recall that E , T , ℓ , and U denote the number of entities, frames, the hierarchical level index, and the kernel width, respectively.

B.3 Network Architecture in Detail

In this section we provide further details regarding the architectural building blocks of MoDi. Some of the description is based on StyleGAN (Karras et al. 2020) and is given here for information completeness.

Generator In Figure 13 we show additional details related to the motion generator. In particular, we depict the usage of modulation and demodulation (Karras et al. 2020), which has been shown to be safer compared to AdaIN (Huang and Belongie 2017) in terms of certain artefacts. The AdaIN block processes *data*, namely normalizes it and applies a new standard deviation. The modulation/demodulation block performs an equivalent (in expectation) operation on the *weights*. Let u denote a weight value within a filter, and let i, j and k denote the input channel index, output channel index, and filter spatial index, respectively. Instead of multiplying the data by a new standard deviation, we *modulate* the weights:

$$u'_{ijk} = s_i \cdot u_{ijk}, \quad (10)$$

and instead of normalizing the data, we *demodulate* the weights:

$$u''_{ijk} = u'_{ijk} / \sqrt{\sum_{i,k} u'_{ijk}^2}. \quad (11)$$

Discriminator Our discriminator, as well as its role in the training procedure, is depicted in Figure 14. Our discriminator holds the reverse architecture of the synthesis network. That is, it receives a generated or real motion, and processes it in neural blocks that gradually decrease in size. Like the motion synthesis network, our discriminator is based on structure-aware neural modules. In each hierarchical level, the skeletal topology becomes coarser using skeletal convolutions.

C Applications – Additional Details

C.1 Inversion – Description of \mathcal{W}^+

Our inversion method uses the \mathcal{W}^+ space. \mathcal{W}^+ is proposed by Abdal, Qin, and Wonka (2019). A tensor in \mathcal{W}^+ is a con-

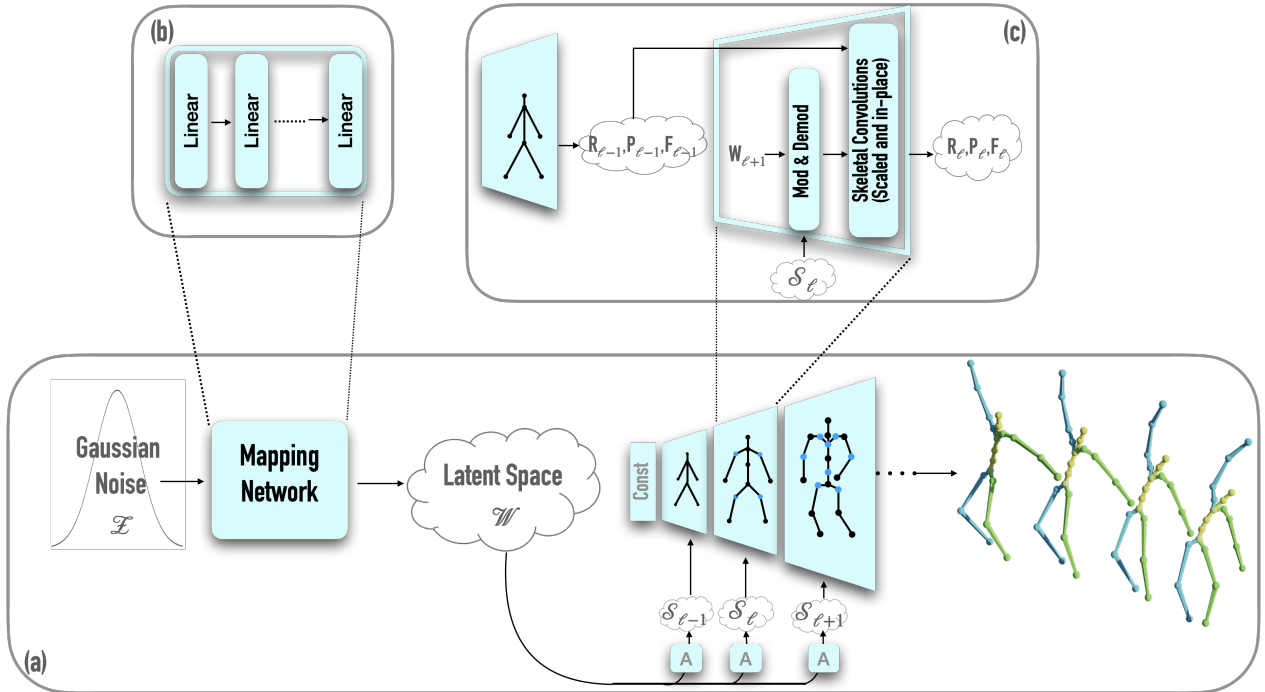


Figure 13: Our motion generator in detail. (a) Adding style injection information to Figure 4 from the main paper. A denotes a learned affine transformation. This transformation is applied on the latent code w to produce a style code \mathcal{S}_ℓ , where ℓ is the hierarchical level index. A different style code is injected to each layer. (b) Zoom in on the mapping network, which is an MLP with several linear layers. (c) Zoom in on the motion synthesis network, where a style code S modulates the layer’s weight. The styled weight is then used for a transposed convolution of the layer features. Recall that \mathbf{R}_ℓ , \mathbf{P}_ℓ and \mathbf{F}_ℓ denote the features in level ℓ of rotations, root positions and foot contact labels, respectively. A transposed skeletal convolution applies the modulated weights on the data features from the previous (coarser) hierarchical level. Since the convolution is transposed, it results with larger dimensions, both in the temporal axis and in the joints axis.

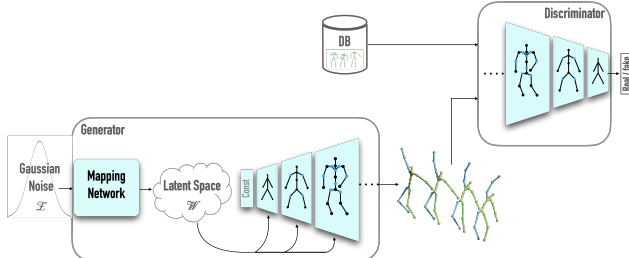


Figure 14: Our discriminator holds the reverse architecture of the synthesis network. It receives a generated or real motion, and learns to output whether the input motion is real or fake. Using structure-aware neural modules, in each hierarchical level the skeletal topology becomes coarser and the number of frames is divided by 2.

catenation of several different $w \in \mathcal{W}$ vectors, one for each layer of the synthesis network. Each vector in \mathcal{W}^+ is used as a modulation input to a different layer. On the other hand, when using \mathcal{W} , the same w vector is used for all layers. Abdal, Qin, and Wonka (2019) show that \mathcal{W} is limited and an inversion from arbitrary images is much more accurate when using \mathcal{W}^+ . In our experiments we have realized that this approach works for the motion domain as well.

C.2 Computing the *gral* score

Our classifier computes the *gral* (gradual right arm lifting) score in the following way. Let $m = [R, S, F]$ be a selected motion. Recall R represents the rotation angles of the motion. Let $R_{rs,t}$ and $R_{re,t}$ denote the rotations of the right shoulder and the right elbow at time t , respectively. Let $[R_{rs,t}, \dots, R_{rs,t+8}]$ be a temporal window of size 8. A similar window is created for R_{re} . We compute the average angle in each window, and slide the window with stride of 4. Altogether we get the average computed $T/4$ times for both the right shoulder and the right elbow. Denote the sequence of average angles by α_{rs} and α_{re} . The next step is to compute the difference between each element to the one preceding it, and obtain

$$score_{rs_i} = \begin{cases} 1, & \text{if } \alpha_{rs_i} > \alpha_{rs_{i-1}}, \\ 0, & \text{otherwise} \end{cases}, \quad (12)$$

$$score_{re_i} = \begin{cases} 1, & \text{if } \alpha_{re_i} > \alpha_{re_{i-1}}, \\ 0, & \text{otherwise} \end{cases}, \quad (13)$$

where $i \in [1, T/4 - 1]$.

Clearly, if all scores are one, the arm is going up, and if they are all zero, the arm is going down. The average of all the values in the two score vectors is used as the final attribute score.

D Experiments – Additional Details

D.1 Datasets

Mixamo – training and evaluation We construct our 3D motion dataset using the Mixamo (Adobe Systems Inc. 2021) 3D animation collection, which contains approximately 2500 extremely diverse motions that are not constrained by any set of categories. These motions are applied on 70 characters. Examples of the motions in the dataset

Name	Hierarchy level	channels × joints × frames
Generator - Motion Synth. Net.	0	256 × 1 × 4
	1	128 × 2 × 8
	2	64 × 7 × 16
	3	64 × 12 × 32
	4	32 × 20 × 64
Discriminator	0	32 × 20 × 64
	1	64 × 12 × 32
	2	64 × 7 × 16
	3	128 × 2 × 8
	4	256 × 1 × 4

Table 3: Architecture: Dimensions of all hierarchy levels.

Name	Neural building blocks
Generator - Motion Synth. Net.	Skeletal Conv. Scaler (upsample)
	Skeletal Conv. (in-place)
	Skeletal Conv. (in-place)
Discriminator	Skeletal Conv. (in-place)
	Skeletal Conv. (in-place)
	Skeletal Conv. Scaler (downsample)
	Add Residual

Table 4: Architecture: Building blocks in hierarchical levels. Skeletal operators are based on (Aberman et al. 2020a).

are elementary actions (jumping, walking), dance moves (samba, hip-hop), martial arts (boxing, capoeira), acrobatics (back/front flips, acrobatic jumps), and non-standard motions (running on a wall, flying).

We generate our data samples by first extracting the relevant edges from each motion (e.g., we drop the fingers). Then we crop each motion to partially overlapping sequences, hence increasing the amount of data.

HumanAct12 – evaluation HumanAct12 (Guo et al. 2020) is not as diverse as Mixamo, and offers approximately 1200 motion clips, organized into 12 action categories and 34 sub-categories. Due to its small number of motions, we use HumanAct12 for quantitative comparison only.

D.2 Hyper-parameters and Training Details

In this section, we describe the details for the network architectures. Table 3 describes the architecture of our generator and discriminator networks. The sizes of the kernels are configurable by hyper-parameters, and in the table we specify which hyper-parameters we have used for our best model. Note that the number of joints varies according to the topology of the skeleton on which the network is trained. The values in Table 3 belong to the skeleton used by the model presented in this work. The structure of each hierarchical level in our generator and discriminator is described in Table 4. A hierarchy level in the motion synthesis network contains input/output skips, and a hierarchy level in the discriminator contains a residual skip, both based on Karras et al. (2020).

In our experiments, we use $\lambda_{fcon} = 1$, $\lambda_{touch} = 0.01$, batch size 16, learning rate 0.002 for both generator and discriminator, mixing 0.9, and train for 80,000 iterations.

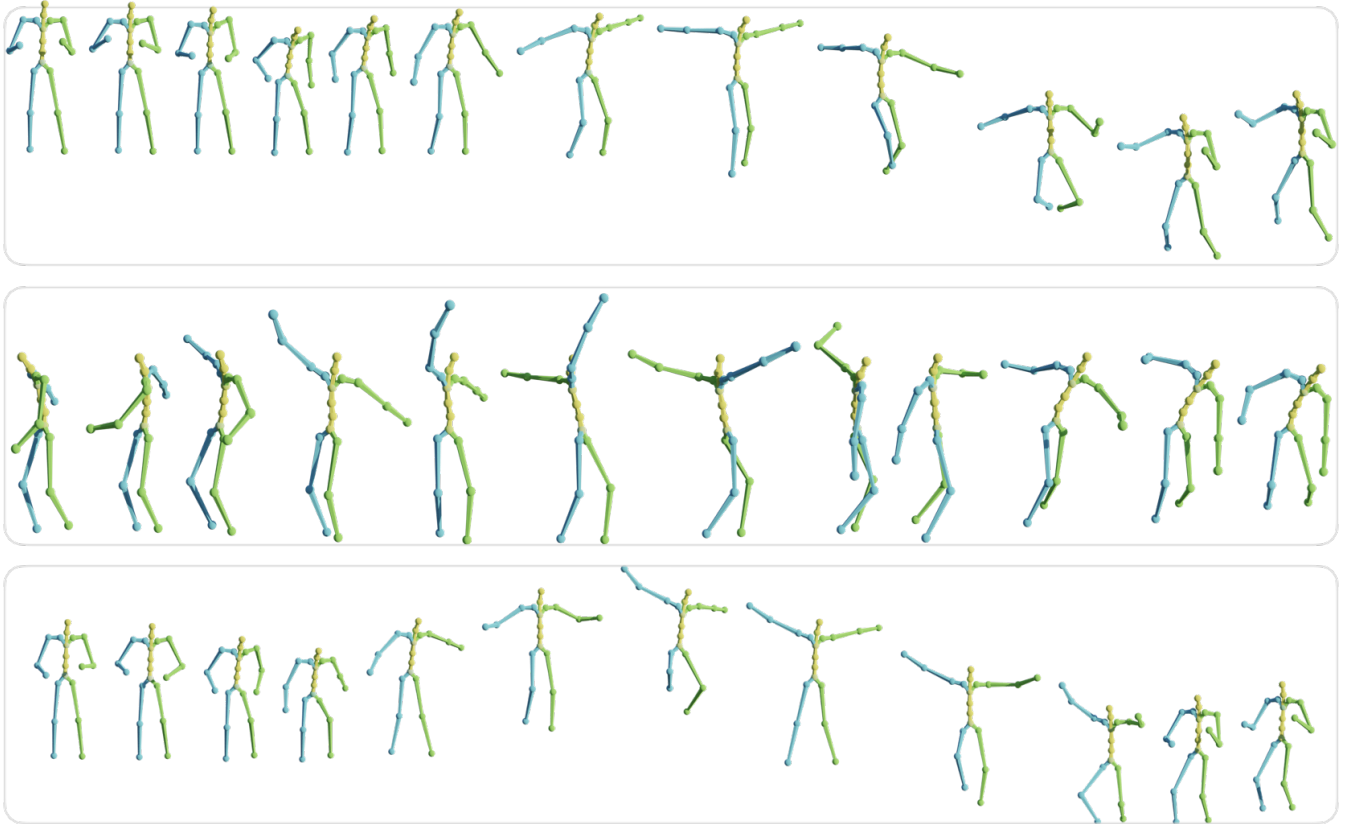


Figure 15: Qualitative results of synthesised jumps and wild dances. See more results in the supplementary video.

We use pytorch version 1.5.0, and CUDA version 10.1 on a GeForce GTX 1080 Ti GPU.

D.3 Quantitative Metrics

We briefly describe each metric that we use for quantitative results.

FID Frèchet inception distance is the distance between the feature distribution of generated motions and that of the real motions, namely the difference in mean and variance. Despite its simplicity, FID is an important metric widely used to evaluate the overall quality of generated motions (Guo et al. 2020; Petrovich, Black, and Varol 2021). FID is borrowed from the image domain, where the inception network is used for features. To adjust this metric to the motion domain, we replace the inception by an action recognition network. A lower value implies better FID results.

KID Kernel Inception Distance (KID), proposed by Bińkowski et al. (2018), compares skewness as well as the values compared in FID, namely mean and variance. KID is known to work better for small and medium size datasets. Lower values are better.

Precision and Recall These measures are adopted from the discriminative domain to the generative domain (Sajjadi et al. 2018). Precision measures the probability that a randomly generated motion falls within the support of the distribution of real images, and is closely related with fidelity. Re-

call measures the probability that a real motion falls within the support of the distribution of generated images, and is closely related with diversity. Higher precision and recall values imply better results.

Diversity This metric measures the variance of generated motions (Guo et al. 2020; Petrovich, Black, and Varol 2021). In the context of action recognition models, it measures the variance across all action categories, and therefore it suits an unconstrained generator. The diversity value is considered good if it is close to the diversity of the ground truth. In all our experiments, the diversity of the generated data was lower than the ground truth, so for clarity we mark it with an upwards pointing arrow, implying that for our case, higher is better.

D.4 Additional Qualitative Results

In Figure 15 we show additional qualitative results. The reader is encouraged to watch the supplementary video in order to get the full impression of our results.

References

- Abdal, R.; Qin, Y.; and Wonka, P. 2019. Image2stylegan: How to embed images into the stylegan latent space? In *Proceedings of the IEEE/CVF International Conference on Computer Vision*, 4432–4441.
- Aberman, K.; Li, P.; Lischinski, D.; Sorkine-Hornung, O.; Cohen-Or, D.; and Chen, B. 2020a. Skeleton-aware networks for deep motion retargeting. *ACM Transactions on Graphics (TOG)*, 39(4): 62–1.
- Aberman, K.; Weng, Y.; Lischinski, D.; Cohen-Or, D.; and Chen, B. 2020b. Unpaired motion style transfer from video to animation. *ACM Transactions on Graphics (TOG)*, 39(4): 64–1.
- Aberman, K.; Wu, R.; Lischinski, D.; Chen, B.; and Cohen-Or, D. 2019. Learning character-agnostic motion for motion retargeting in 2d. *arXiv preprint arXiv:1905.01680*.
- Adobe Systems Inc. 2021. Mixamo. Accessed: 2021-12-25.
- Aksan, E.; Kaufmann, M.; and Hilliges, O. 2019. Structured prediction helps 3d human motion modelling. In *Proceedings of the IEEE/CVF International Conference on Computer Vision*, 7144–7153. IEEE Computer Society.
- Aristidou, A.; Yiannakidis, A.; Aberman, K.; Cohen-Or, D.; Shamir, A.; and Chrysanthou, Y. 2021. Rhythm is a Dancer: Music-Driven Motion Synthesis with Global Structure. *arXiv preprint arXiv:2111.12159*.
- Barsoum, E.; Kender, J.; and Liu, Z. 2018. Hp-gan: Probabilistic 3d human motion prediction via gan. In *Proceedings of the IEEE conference on computer vision and pattern recognition workshops*, 1418–1427.
- Bermano, A. H.; Gal, R.; Alaluf, Y.; Mokady, R.; Nitzan, Y.; Tov, O.; Patashnik, O.; and Cohen-Or, D. 2022. State-of-the-Art in the Architecture, Methods and Applications of StyleGAN. In *Computer Graphics Forum*, volume 41, 591–611. Wiley Online Library.
- Biswas, S.; Yin, K.; Shugrina, M.; Fidler, S.; and Khamis, S. 2021. Hierarchical Neural Implicit Pose Network for Animation and Motion Retargeting. *arXiv preprint arXiv:2112.00958*.
- Bińkowski, M.; Sutherland, D. J.; Arbel, M.; and Gretton, A. 2018. Demystifying MMD GANs. In *International Conference on Learning Representations*.
- Brock, A.; Donahue, J.; and Simonyan, K. 2018. Large scale GAN training for high fidelity natural image synthesis. *arXiv preprint arXiv:1809.11096*.
- Degardin, B.; Neves, J.; Lopes, V.; Brito, J.; Yaghoubi, E.; and Proença, H. 2022. Generative Adversarial Graph Convolutional Networks for Human Action Synthesis. In *Proceedings of the IEEE/CVF Winter Conference on Applications of Computer Vision*, 1150–1159. Los Alamitos, CA, USA: IEEE Computer Society.
- Duan, Y.; Shi, T.; Zou, Z.; Lin, Y.; Qian, Z.; Zhang, B.; and Yuan, Y. 2021. Single-shot motion completion with transformer. *arXiv preprint arXiv:2103.00776*.
- Fragkiadaki, K.; Levine, S.; Felsen, P.; and Malik, J. 2015. Recurrent network models for human dynamics. In *Proceedings of the IEEE International Conference on Computer Vision*, 4346–4354. IEEE Computer Society.
- Ghorbani, S.; Wloka, C.; Etemad, A.; Brubaker, M. A.; and Troje, N. F. 2020. Probabilistic Character Motion Synthesis using a Hierarchical Deep Latent Variable Model. *Computer Graphics Forum*.
- Goodfellow, I.; Pouget-Abadie, J.; Mirza, M.; Xu, B.; Warde-Farley, D.; Ozair, S.; Courville, A.; and Bengio, Y. 2014. Generative adversarial nets. *Advances in neural information processing systems*, 27.
- Guo, C.; Zuo, X.; Wang, S.; Zou, S.; Sun, Q.; Deng, A.; Gong, M.; and Cheng, L. 2020. Action2motion: Conditioned generation of 3d human motions. In *Proceedings of the 28th ACM International Conference on Multimedia*, 2021–2029. ACM New York, NY, USA.
- Habibie, I.; Holden, D.; Schwarz, J.; Yearsley, J.; and Komura, T. 2017. A recurrent variational autoencoder for human motion synthesis. In *28th British Machine Vision Conference*.
- Harvey, F. G.; and Pal, C. 2018. Recurrent transition networks for character locomotion. In *SIGGRAPH Asia 2018 Technical Briefs*, 1–4.
- Harvey, F. G.; Yurick, M.; Nowrouzezahrai, D.; and Pal, C. 2020. Robust motion in-betweening. *ACM Transactions on Graphics (TOG)*, 39(4): 60–1.
- Hernandez, A.; Gall, J.; and Moreno-Noguer, F. 2019. Human motion prediction via spatio-temporal inpainting. In *Proceedings of the IEEE/CVF International Conference on Computer Vision*, 7134–7143. IEEE Computer Society.
- Ho, J.; Jain, A.; and Abbeel, P. 2020. Denoising diffusion probabilistic models. *Advances in Neural Information Processing Systems*, 33: 6840–6851.
- Holden, D.; Habibie, I.; Kusajima, I.; and Komura, T. 2017. Fast neural style transfer for motion data. *IEEE computer graphics and applications*, 37(4): 42–49.
- Holden, D.; Komura, T.; and Saito, J. 2017. Phase-functioned neural networks for character control. *ACM Transactions on Graphics (TOG)*, 36(4): 1–13.
- Holden, D.; Saito, J.; and Komura, T. 2016. A deep learning framework for character motion synthesis and editing. *ACM Transactions on Graphics (TOG)*, 35(4): 1–11.
- Holden, D.; Saito, J.; Komura, T.; and Joyce, T. 2015. Learning motion manifolds with convolutional autoencoders. In *SIGGRAPH Asia 2015 technical briefs*, 1–4.
- Huang, X.; and Belongie, S. 2017. Arbitrary style transfer in real-time with adaptive instance normalization. In *Proceedings of the IEEE international conference on computer vision*, 1501–1510.
- Jang, D.-K.; and Lee, S.-H. 2020. Constructing human motion manifold with sequential networks. In *Computer Graphics Forum*, volume 39, 314–324. Wiley Online Library.
- Karras, T.; Aittala, M.; Laine, S.; Härkönen, E.; Hellsten, J.; Lehtinen, J.; and Aila, T. 2021. Alias-free generative adversarial networks. *Advances in Neural Information Processing Systems*, 34.
- Karras, T.; Laine, S.; Aittala, M.; Hellsten, J.; Lehtinen, J.; and Aila, T. 2020. Analyzing and improving the image quality of stylegan. In *Proceedings of the IEEE/CVF Conference on Computer Vision and Pattern Recognition*, 8110–8119.

- Kaufmann, M.; Aksan, E.; Song, J.; Pece, F.; Ziegler, R.; and Hilliges, O. 2020. Convolutional autoencoders for human motion infilling. In *2020 International Conference on 3D Vision (3DV)*, 918–927. IEEE.
- Kingma, D. P.; and Dhariwal, P. 2018. Glow: Generative flow with invertible 1x1 convolutions. *Advances in neural information processing systems*, 31.
- Lee, J.; Kim, S.; and Lee, K. 2018. Listen to dance: Music-driven choreography generation using autoregressive encoder-decoder network. *arXiv preprint arXiv:1811.00818*.
- Li, P.; Aberman, K.; Zhang, Z.; Hanocka, R.; and Sorkine-Hornung, O. 2022. GANimator: Neural Motion Synthesis from a Single Sequence. *ACM Transactions on Graphics (TOG)*, 41(4): 138.
- Li, R.; Yang, S.; Ross, D. A.; and Kanazawa, A. 2021. Learn to dance with aist++: Music conditioned 3d dance generation. *arXiv e-prints*, arXiv-2101.
- Maheshwari, S.; Gupta, D.; and Sarvadevabhatla, R. K. 2022. MUGL: Large Scale Multi Person Conditional Action Generation with Locomotion. In *Proceedings of the IEEE/CVF Winter Conference on Applications of Computer Vision*, 257–265. Los Alamitos, CA, USA: IEEE Computer Society.
- Mescheder, L.; Geiger, A.; and Nowozin, S. 2018. Which Training Methods for GANs do actually Converge? In *International Conference on Machine learning (ICML)*.
- Nitzan, Y.; Gal, R.; Brenner, O.; and Cohen-Or, D. 2021. LARGE: Latent-Based Regression through GAN Semantics. *arXiv preprint arXiv:2107.11186*.
- Petrovich, M.; Black, M. J.; and Varol, G. 2021. Action-conditioned 3D human motion synthesis with transformer VAE. In *Proceedings of the IEEE/CVF International Conference on Computer Vision*, 10985–10995. IEEE Computer Society.
- Reimers, N.; and Gurevych, I. 2019. Sentence-BERT: Sentence Embeddings using Siamese BERT-Networks. In *Proceedings of the 2019 Conference on Empirical Methods in Natural Language Processing and the 9th International Joint Conference on Natural Language Processing (EMNLP-IJCNLP)*, 3982–3992.
- Sajjadi, M. S.; Bachem, O.; Lucic, M.; Bousquet, O.; and Gelly, S. 2018. Assessing generative models via precision and recall. *Advances in Neural Information Processing Systems*, 31.
- Shen, Y.; Yang, C.; Tang, X.; and Zhou, B. 2020. InterFaceGAN: Interpreting the Disentangled Face Representation Learned by GANs. *arXiv preprint arXiv:2005.09635*.
- Shi, M.; Aberman, K.; Aristidou, A.; Komura, T.; Lischinski, D.; Cohen-Or, D.; and Chen, B. 2020. Motionet: 3d human motion reconstruction from monocular video with skeleton consistency. *ACM Transactions on Graphics (TOG)*, 40(1): 1–15.
- Sun, G.; Wong, Y.; Cheng, Z.; Kankanhalli, M. S.; Geng, W.; and Li, X. 2020. DeepDance: music-to-dance motion choreography with adversarial learning. *IEEE Transactions on Multimedia*, 23: 497–509.
- Tevet, G.; Gordon, B.; Hertz, A.; Bermano, A. H.; and Cohen-Or, D. 2022. MotionCLIP: Exposing Human Motion Generation to CLIP Space. *arXiv preprint arXiv:2203.08063*.
- Villegas, R.; Yang, J.; Ceylan, D.; and Lee, H. 2018. Neural kinematic networks for unsupervised motion retargetting. In *Proceedings of the IEEE Conference on Computer Vision and Pattern Recognition*, 8639–8648.
- Wang, Q.; Artières, T.; Chen, M.; and Denoyer, L. 2020a. Adversarial learning for modeling human motion. *The Visual Computer*, 36(1): 141–160.
- Wang, Z.; Yu, P.; Zhao, Y.; Zhang, R.; Zhou, Y.; Yuan, J.; and Chen, C. 2020b. Learning diverse stochastic human-action generators by learning smooth latent transitions. In *Proceedings of the AAAI conference on artificial intelligence*, volume 34, 12281–12288.
- Yan, S.; Li, Z.; Xiong, Y.; Yan, H.; and Lin, D. 2019. Convolutional sequence generation for skeleton-based action synthesis. In *Proceedings of the IEEE/CVF International Conference on Computer Vision*, 4394–4402. IEEE Computer Society.
- Yan, S.; Xiong, Y.; and Lin, D. 2018. Spatial temporal graph convolutional networks for skeleton-based action recognition. In *Thirty-second AAAI conference on artificial intelligence*.
- Yang, Z.; Li, Y.; Yang, J.; and Luo, J. 2018. Action recognition with spatio-temporal visual attention on skeleton image sequences. *IEEE Transactions on Circuits and Systems for Video Technology*, 29(8): 2405–2415.
- Yu, P.; Zhao, Y.; Li, C.; Yuan, J.; and Chen, C. 2020. Structure-aware human-action generation. In *European Conference on Computer Vision*, 18–34. Springer.
- Yuan, Y.; and Kitani, K. 2020. Dlow: Diversifying latent flows for diverse human motion prediction. In *European Conference on Computer Vision*, 346–364. Springer.
- Zhang, J.-Q.; Xu, X.; Shen, Z.-M.; Huang, Z.-H.; Zhao, Y.; Cao, Y.-P.; Wan, P.; and Wang, M. 2021. Write-Animation: High-level Text-based Animation Editing with Character-Scene Interaction. In *Computer Graphics Forum*, volume 40, 217–228. Wiley Online Library.
- Zhang, Y.; Black, M. J.; and Tang, S. 2021. We are more than our joints: Predicting how 3d bodies move. In *Proceedings of the IEEE/CVF Conference on Computer Vision and Pattern Recognition*, 3372–3382.
- Zhou, Y.; Li, Z.; Xiao, S.; He, C.; Huang, Z.; and Li, H. 2018. Auto-Conditioned Recurrent Networks for Extended Complex Human Motion Synthesis. In *International Conference on Learning Representations*.